Structure of monolayer 2H-TaS$_2$ on Au(111)

Caio C. Silva [1,2] Daniela Dombrowski,[1,3] Abdus Samad,[4] Jiaqi Cai,[1,3] Wouter Jolie [5] Joshua Hall,[5] Paul T. P. Ryan,[2,6]
Pardeep K. Thakur [2] David A. Duncan,[2] Tien-Lin Lee,[2] Udo Schwingenschlögl,[4] and Carsten Busse [1,3,*]

[1]*Institut für Materialphysik, Westfälische Wilhelms-Universität Münster, Wilhelm-Klemm-Straße 10, D-48149 Münster, Germany*
[2]*Diamond Light Source, Didcot OX11 0DE, United Kingdom*
[3]*Department Physik, Universität Siegen, Walter-Flex-Straße 3, D-57068 Siegen, Germany*
[4]*King Abdullah University of Science and Technology (KAUST), Physical Science and Engineering Division (PSE),
Thuwal 23955-6900, Saudi-Arabia*
[5]*II. Physikalisches Institut, Universität zu Köln, Zülpicher Straße 77, D-50937 Köln, Germany*
[6]*Department of Materials, Imperial College London, Exhibition Road, SW7 2AZ London, United Kingdom*

We determined the structure of epitaxial 2H-TaS$_2$ on Au(111) using the method of x-ray standing waves (XSW), supported by density functional theory (DFT) calculations and scanning tunneling microscopy (STM). The lattice mismatch between substrate and overlayer gives rise to a moiré superstructure, which modulates the structural and electronic properties. For a specific registry (S atoms directly above Au substrate atoms), local covalentlike bonds form, whereas globally weak van der Waals bonding prevails. Still, the TaS$_2$ layer remains rather flat. Significant charge transfer from Au(111) into the conduction band of the two-dimensional material is found.

I. INTRODUCTION

Monolayers of transition metal dichalcogenides (TMDCs) with the general composition MX$_2$ (M, transition metal; X, S, Se, Te) are a particularly rich family of two-dimensional materials (2DMs), comprising insulators, semiconductors, and metals [1]. Metallic TMDC compounds (M=V, Nb, Ta) are especially interesting as they are suitable as atomically thin electrical contacts [2] and catalysts for the hydrogen evolution reaction (HER) [3]. On fundamental grounds, two-dimensional metals are prone to electronic instabilities as charge-density waves (CDW)[4–6] that can potentially even lead to spin polarization [7].

Modification by the presence of a substrate is a common feature of 2DMs, which is even more pronounced for metallic compounds that typically interact stronger with their environment than semiconducting ones [8]. The interaction broadens and shifts the electronic states of the 2DM [8], and differences in work function drive charge transfer, leading to doping. Overlap of bands causes hybridization [9], and, in addition to the overall van der Waals interaction, localized chemical bonds may form. The charge carriers in the ultrathin sheet can be influenced by interfacial electrostatic interactions [6]. All these effects can be exploited to tune the properties of the 2DM in a desired way (contact engineering). On top of this, the commonly found lattice mismatch between overlayer and substrate can lead to a moiré superstructure that can modulate structural [10] as well as electronic [11] properties.

TaS$_2$, the material in focus here, can be found in the typical polymorphs of TMDCs, namely 1T, where the metal ions are found in an octahedral coordination and 2H, where it sits in a trigonal prismatic environment (note that some authors denote the latter as 1H when monolayers are concerned). Well-ordered and defect-free monolayers of 2H-TaS$_2$ can be obtained by reactive molecular beam epitaxy (MBE) using the inert Au(111) surface as a substrate [12]. However, the remaining interaction can still be strong enough to severely influence the properties of TaS$_2$ by epitaxial strain, doping [13], hybridization of Au bands [9], and strong local covalentlike Au-S bonds [14]. Specifically, the presence of the gold substrate destroys the charge density wave order [12], which prevails on the less interacting substrate graphene [5], and is even enhanced on hexagonal boron nitride (hBN) by interfacial electrostatic interactions [6]. Furthermore, the presence of the gold substrate can stabilize sulfur-poor phases of monolayer tantalum sulfide [15].

A detailed analysis of the geometric structure of TaS$_2$/Au(111) is mandatory in order to understand the interaction between overlayer and substrate with the goal to disentangle the different aspects. Here, we employ x-ray standing waves (XSW) for a precise determination of the vertical arrangement of the atoms, corroborated by scanning tunneling microscopy (STM) and density functional theory (DFT).

II. EXPERIMENTAL METHODS

We used two ultrahigh vacuum (UHV) systems located in Münster (MS, background pressure $p = 5 \times 10^{-11}$ mbar) and

*carsten.busse@uni-siegen.de

at the beamline I09 of Diamond Light Source, Didcot, UK (DLS, $p = 2 \times 10^{-10}$ mbar).

Au(111) was prepared through cycles of irradiation with Ar^+ ions (DLS: 1.0 keV/MS: 1.5 keV) and annealing up to 875 K/900 K until a low-energy electron diffraction (LEED) pattern typical of the herringbone reconstruction $(22 \times \sqrt{3})$ was obtained (DLS) or no impurities were visible in STM (MS). Monolayer $2H$-TaS_2 was grown by reactive MBE following Refs. [16,17]: Ta was evaporated from an e-beam evaporator (EGCO4, Oxford Applied Instruments) with a rate of ≈ 0.02 ML/min (calibrated with a quartz crystal microbalance) (DLS) or a rate of ≈ 0.07 ML/min (calibrated with STM) (MS), with the sample at room temperature, for 5 min/3.5 min. Here, 1 ML refers to full coverage of the Au(111) surface with a pseudomorphic layer of Ta. In parallel, the sample was exposed to H_2S using a tube with 1.2 cm/1 cm diameter ending 2 cm/3 cm in front of the sample. The background pressure during this exposure is 1×10^{-5} mbar/1×10^{-7} mbar. Evaporation was stopped and the sample was heated for 30 min/20 min at 875 K/850 K while the exposure to H_2S was continued. At DLS, this procedure was performed twice to obtain a high coverage film. A preceding detailed study of the growth parameters showed that under these conditions, exclusively monolayers of the $2H$-TaS_2 result [15]. We observed the same LEED pattern in both systems, using a standard optics in MS and a microchannel plate at DLS.

STM (MS) was performed *in situ* at room temperature. For x-ray photoelectron spectroscopy (XPS) and XSW at DLS, we used a hemispherical electron analyzer (VG Scienta EW4000) with an angular acceptance of $56°$. X-ray reflectivity is measured using an image of a fluorescent screen obtained with a CCD camera.

All components in the photoemission spectra were fitted using Doniach-Sunjic line shapes [18] convoluted with a Gaussian function after a Shirley background subtraction [19]. The binding energy difference between the components found in the fitting processes of XPS were used for reference in the XSW analysis.

XSW is an experimental technique which provides a precise determination of the distance between an adsorbate and the surface substrate [20–22]. This technique has been successfully applied to clarify structural aspects of epitaxially grown 2DMs [10,23–30]. Basically, the x-ray standing wave field is formed as a consequence of the coherent superposition of the incoming x-ray wave and the reflected one at the Bragg condition. The resulting standing wave will have a periodicity that matches that of the layer spacing between the Bragg diffraction planes [31]. As one scans across the Bragg condition, e.g., by varying the incident photon energy, the phase of this standing wave will vary by π. When looking at diffraction from an fcc crystal containing a single element (e.g., Au), this results in the antinodes of the standing wave varying in position from halfway between the Bragg diffraction planes, down to being coincident with those planes. Thus, the absorption of the XSW by an adsorbed atom as a function of the incident photon energy differs significantly due to its specific height (e.g., [32]). The analysis of the photoelectron yield during the energy scan gives information about the height of the adsorbate.

The photoelectron yield can be uniquely fitted using dynamical diffraction theory [33], resulting in two structural parameters: the coherent position (P^H) and the coherent fraction (f^H) [20]. P^H is the average height of all atoms of the analyzed species and f^H indicates the distribution of atoms around this mean height ($f^H = 1$ for a δ-like distribution). The average height of a species is given by $\bar{h} = (P^H + n) \times d_{Au(111)}$, where $d_{Au(111)} = 2.3545$ Å [34] is the Bragg plane spacing of Au(111). The integer n stems from the fact that the XSW field is periodic and in principle leads to a modulo-$d_{Au(111)}$ ambiguity for the determination of heights using XSW. However, the value of n can be easily determined using complementary experimental or theoretical results or simply the atomic radii of the atoms. All the distances measured through XSW analysis are presented with errors [35].

To perform spin-degenerate DFT calculations we used the Vienna *ab initio* Simulation Package (projector augmented wave method) [36]. The generalized gradient approximation was applied to the exchange correlation potential using the Perdew-Burke-Ernzerhof functional [37]. We used the valence electron configurations Ta $5p^6 6s^2 6d^3$, S $3s^2 3p^4$, and Au $5d^{10}6s^1$. An energy cutoff of 360 eV was employed for the plane-wave basis. For the supercells of $7 \times 7 \times 1$ $2H$-TaS_2 in contact with $8 \times 8 \times 1$ Au(111) (4 Au layers) a $2 \times 2 \times 1$ k mesh was used. Slab models were obtained by adding a vacuum layer of 15 Å starting at the edge of the slab in the out-of-plane direction. The two Au layers farthest away from the interface were fixed at the atomic positions of bulk Au. The total energy convergence criterion of the self-consistency calculations was set to 10^{-6} eV. The atomic positions and lattice constants were optimized until the Hellmann-Feynman forces remained below 10^{-2} eV/Å and the remaining pressure was reduced to less than 1 kbar. The Grimme semiempirical method was used for the van der Waals correction [38]. To derive P^H and f^H from the calculated coordinates, we took the upper fixed Au layer as the reference and used the experimental value of $d_{Au(111)}$. Charge transfer between $2H$-TaS_2 and the substrate was determined by a Bader charge analysis [39].

III. RESULTS AND DISCUSSION

The LEED pattern of TaS_2/Au(111) (inset of Fig. 1) exhibits the characteristic moiré superstructure resulting from the lattice mismatch. The diffraction spots of Au(111) and TaS_2 are well aligned. The moiré superstructure is also reflected in the height modulation ($\Delta h_{STM} = (0.4 \pm 0.1)$ Å) in the STM topograph (Fig. 1). We find almost perfect alignment between the atomic and the moiré lattice, which indicates that TaS_2 follows the orientation of the underlying substrate.

The moiré unit cell (white rhombus in Fig. 1) can be described as $[m \times m]$ unit cells of TaS_2 on $[(m + 1) \times (m + 1)]$ unit cells of Au(111). By counting along lines of different orientation and in several images we determine $m = 6.9 \pm 0.2$. In consequence, for theoretical modeling (see below) a structure of $(7 \times 7)_{TaS_2}/(8 \times 8)_{Au(111)}$ is recommended. A moiré analysis [40,41] leads to a TaS_2 lattice parameter of $a_{TaS_2} = (3.30 \pm 0.01)$ Å.

The experimental value for a_{TaS_2} is smaller than the one found for TaS_2 grown on the more weakly interacting substrate graphene ((3.37 ± 0.02) Å for graphene on Ir(111)
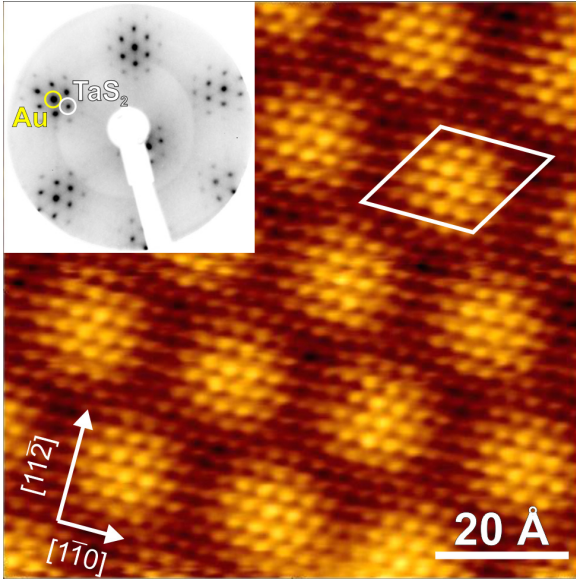
FIG. 1. High-resolution STM image of the moiré lattice of TaS$_2$/Au(111). The unit cell is indicated by a white rhombus. Tunneling conditions are as follows: $U_{\mathrm{sample}} = -0.2$ V, $I_{\mathrm{tunnel}} = 3.3$ nA. (Inset) Corresponding LEED pattern (inverted contrast, electron energy 80.5 eV) obtained at DLS. Characteristic spots of Au and TaS$_2$ are marked.

TABLE I. Key parameters of the components observed in photoemission. Spin-orbit-splitting Δ_{so}, name and color code of the component (see Fig. 2), binding energy E_{B}, full width at half maximum (FWHM) Γ, and asymmetry parameter for Doniach-Sunjic function α. Errors in the energy determination were estimated as ± 0.02 eV.

Core level	Δ_{so}	Comp.	Color	E_{B} (eV)	Γ (eV)	α
Ta 4$f_{7/2}$	1.89	Ta	blue	22.72	0.24	0.14
		Ta$'$	green	23.39	0.23	0.07
		Ta$''$	red	23.75	0.37	0.10
S 2$p_{3/2}$	1.20	S2	blue	160.83	0.31	0.07
		S1	green	161.41	0.50	0.07

XPS data measured with an incident photon energy around the Bragg energy for Au(111) of $E_{\mathrm{Bragg}} = 2.635$ keV (a necessary condition for XSW measurements). An XSW analysis of the photoelectron yields for the main Ta 4$f_{7/2}$ peak and the S 2$p_{3/2}$ peak is presented in Fig. 3. The resulting structural parameters coherent position P^H and coherent fraction f^H of the main components are shown in Table II together with the results from theory (see below).

using STM [5], 3.40 Å for graphene on SiC using RHEED [4]). It is possible that the smaller lattice constant on Au(111) is caused by strain and/or charge transfer from the substrate (see below).

Figure 2 shows the high-resolution XPS of the core levels Ta 4f [Fig. 2(a)] and S 2p [Fig. 2(b)]. Both core levels show spin-orbit splitting, resulting in the doublets Ta 4$f_{7/2}$ - Ta 4$f_{5/2}$ and S 2$p_{3/2}$ - S 2$p_{1/2}$. We find three components for the case of Ta 4f and two for the case of S 2p; selected fitting parameters are given in Table I. The spin-orbit splitting values were obtained from the component fitting process.

The same fitting model used in the high-resolution XPS data presented in Fig. 2 was used to fit the lower resolution
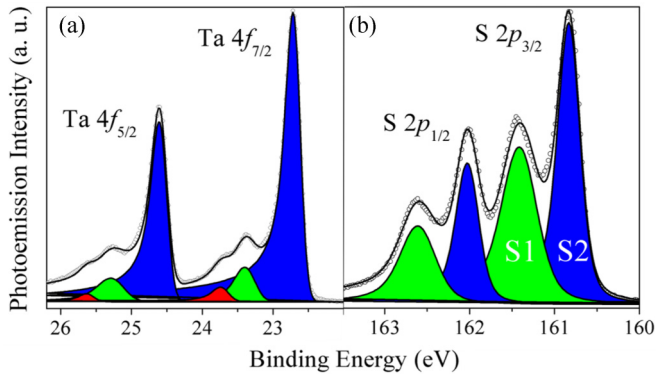

FIG. 2. (a) X-ray photoemission spectrum of Ta 4f measured with $h\nu = 150$ eV. (b) X-ray photoemission spectrum of S 2p measured with $h\nu = 360$ eV. (Circles) Data points after background subtraction. (Colored areas) Fits of the indicated components (see Table I). (Solid black line) Sum of fits.
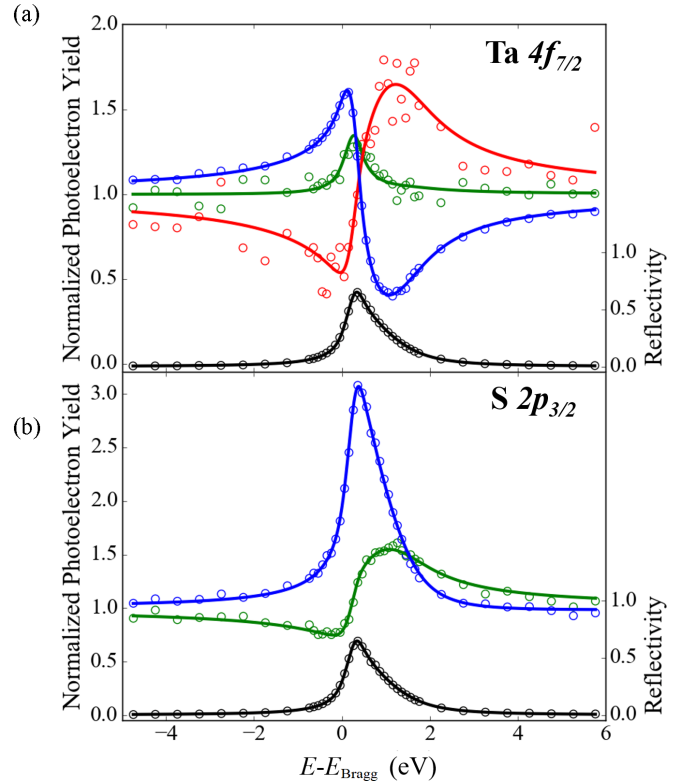

FIG. 3. XSW analysis for (a) XPS components of Ta 4f [Figs. 2(a) and 2(b)] XPS components of S 2p [Fig. 2(b)]. The XSW profiles (blue, green, red) show the variation in total photoelectron yield as a function of the photon energy scan around the Bragg energy of $E_{\mathrm{Bragg}} = 2.635$ keV for Au(111). The colors denote the components as defined in Fig. 2; see also Table I. The x-ray reflectivity is shown in black. The experimental data is shown as open circles and the best fit from dynamical diffraction theory [33] is shown as solid lines.

TABLE II. Comparison between the structural parameters P^H and f^H obtained from XSW and DFT structures. For the XSW results, errors were estimated by the method of Mercurio *et al.* [35] resulting in $\Delta P^H = \pm 0.03$ and $\Delta f^H = \pm 0.04$.

	S1		Ta		S2	
	P^H	f^H	P^H	f^H	P^H	f^H
XSW	**0.07**	0.52	**0.74**	0.82	**0.39**	0.77
DFT	***0.04***	*0.97*	***0.70***	*0.96*	***0.36***	*0.96*

We attribute the main component in the Ta $4f_{7/2}$ peak [blue in Fig. 2(a)] to the Ta layer in the basal plane of TaS_2. The minority components (Ta′, green, $P^H = 0.86$, $F^H = 0.29$; and Ta″, red, $P^H = 0.07$, $F^H = 0.75$) are related to Ta impurities resulting from the growth process. For the most intense component a direct interpretation of the coherent position is possible: $P^H = 0.74 \pm 0.02$ yields a mean Ta height of (4.09 ± 0.04) Å (the heights extracted from XSW are referenced to the virtual unrelaxed surface).

Assuming that the component S2 of S $2p_{3/2}$ [blue in Fig. 2(b)] is connected to the upper S layer in TaS_2, the XSW analysis results in a height of (5.62 ± 0.05) Å. Following this assumption, the component S1 of S $2p_{3/2}$ [green in Fig. 2(b)] is assigned to the lower S layer in TaS_2. Therefore, from the XSW analysis, the S1 layer is found at (2.51 ± 0.05) Å.

The values found for f^H are more difficult to interpret. First, whereas P^H as a measure of the average position of the atoms is fairly robust against impurities or a few falsely assigned atoms, f^H as a measure of the width of the distribution depends on such deviations more sensitively. The observed f^H can thus only give an upper bound for the contribution of the geometric structure to the overall width. Second, for a quantitative interpretation, one has to put in a model of the geometric structure. A realistic but still analytically solvable model for 2DMs with a hexagonal moiré superstructure is the eggbox model [23], more formal a layer of p6m symmetry with Fourier components up to first order only. In this model, f^H can be calculated from the peak-to-peak corrugation amplitude Δh of the eggbox; see Fig. 4 of Ref. [23]. Here, we use f^H of Ta as a representative of the corrugation of TaS_2, as this component is less susceptible to potential errors in fitting the photoemission spectra than the S components that overlap with each other. The high value of $f^H = 0.82 \pm 0.04$ then implies a rather low peak-to-peak corrugation of $\Delta h_{XSW} = (0.8 \pm 0.1)$ Å. In view of the uncertainties connected to f^H, this value should be interpreted conservatively as an upper bound of the corrugation amplitude.

To corroborate our experimental results and to elucidate details of the geometric and electronic structure we performed DFT calculations. We use the closest commensurate approximation to the experimentally determined structure, namely a 7-on-8 geometry. Under the constraint that the lattice vectors of TaS_2 are aligned with the dense-packed directions of Au(111) there are two possible stackings: The $[2\bar{1}\bar{1}0]$ direction of TaS_2 (zigzag direction) can either be aligned with the dense-packed $[1\bar{1}0]$ direction of Au(111) or rotated against it by $60°$, i.e., aligned with the $[10\bar{1}]$ direction. Note that $[1\bar{1}0]$ and $[10\bar{1}]$ are not equivalent: When you follow $[1\bar{1}0]$ with

TABLE III. Structural parameters obtained by DFT for the two possible stackings. (E_b) Binding energy per TaS_2 unit cell referenced to a system comprising a free-standing 2D layer and the pristine substrate; a lower value describes a more stable structure. (ΔE_b) Binding energy difference with respect to the most stable stacking. Mean height $\bar{h}$, minimum height h_{min}, maximum height h_{max}, and corrugation $\Delta h = h_{max} - h_{min}$ of the atoms in the lower (S1) and upper (S2) sulfur layer as well as the Ta layer, referenced to the topmost Au layer. All values in Å.

	$Ta_{fcc}S_{top}$			$Ta_{hcp}S_{top}$		
E_b	−874.0 meV			−871.1 meV		
ΔE_b	0 meV			2.9 meV		
	S1	Ta	S2	S1	Ta	S2
$\bar{h}$	2.42	3.95	5.48	2.42	3.95	5.48
h_{min}	2.25	3.77	5.30	2.22	3.76	5.26
h_{max}	2.54	4.10	5.64	2.54	4.10	5.63
Δh	0.29	0.33	0.33	0.33	0.34	0.37

your head pointing along [111] and cross a bridge site, you have an hcp site to your left and an fcc site to your right. This is reversed for $[10\bar{1}]$. In consequence, also the stacking of TaS_2 with respect to Au(111) is different.

We calculated both possible stackings. The energetically favorable structure (see Table III) is shown in Fig. 4. There are three regions of high local symmetry that we label according to the positions of the constituents as $Ta_{fcc}S_{top}$, $Ta_{hcp}S_{fcc}$, and

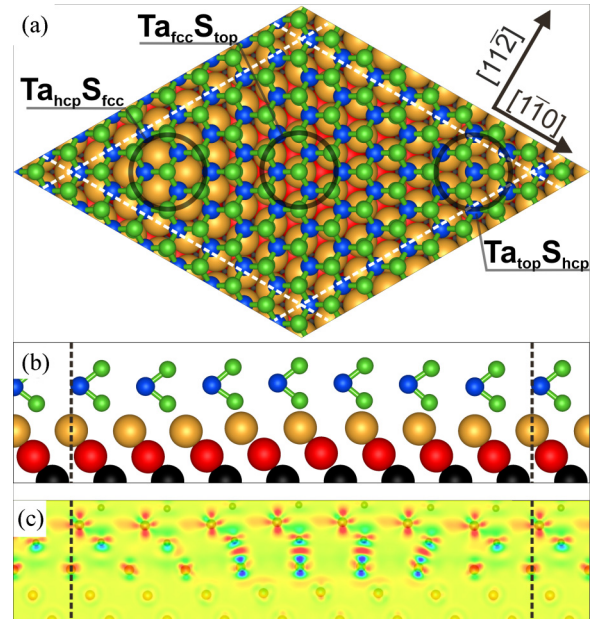FIG. 4. Relaxed structure of TaS_2/Au(111) with 7×7 TaS_2 unit cells on 8×8 Au(111) unit cells in the $Ta_{fcc}S_{top}$-stacking. S atoms are colored green, Ta atoms blue, and Au atoms in different layers gold, red, and black. Dashed lines indicate the unit cell. Regions of high symmetry are labeled. (a) Top view. (b) Side view along a cut following the main diagonal. (c) 2D color gradient plot of the charge density difference upon adsorption along the same plane as shown in (b). (Blue) Minimum ($-16.7 \times 10^{-3}e^-/Å^3$) (electron depletion); (red) maximum ($6.6 \times 10^{-3}e^-/Å^3$) (electron accumulation).

Ta$_{top}$S$_{hcp}$. For the alternative stacking (not shown here), the respective regions are Ta$_{hcp}$S$_{top}$, Ta$_{fcc}$S$_{hcp}$, and Ta$_{top}$S$_{fcc}$. We use the region where S is on top of an Au(111) atom as a representation of the stacking and hence denote the two orientations as Ta$_{fcc}$S$_{top}$ and Ta$_{hcp}$S$_{top}$. This nomenclature is motivated by the finding that in these regions the S-Au distance is minimal (see below) and hence the local interaction is strongest.

The energy difference between the two rotational variants is rather small ($\Delta E_b = 2.9$ meV per unit cell). For comparison, hBN/Ir(111) [26] can also exist in two domains with a similar energy difference ($\Delta E_b = 2.8$ meV per unit cell). This hints at a general problem to achieve phase-pure 2DMs on fcc(111) surfaces. A previous DFT study using a simplified system found a similar absolute value of the binding energy of -820 meV per TaS$_2$ unit cell [8]. This binding energy is a factor of five larger than found for graphene and hBN on Ir(111) [26].

In our experiment, both types of stacking could be present. In addition, growth can in principle take place on the fcc areas of the Au(111) herringbone reconstruction (as assumed in our DFT model) as well as on the hcp areas. However, we expect that the resulting structures are very similar to those found on the fcc areas, as they only differ in the stacking of the third Au layer. To simplify, we assume that in experiment we measure an average of the structures determined by DFT. A straightforward way to compare theory and experiment is to calculate the structural parameters P^H and f^H from the DFT model (see Table II). We find that these parameters do not differ in the first two significant digits for both types of stackings, so we do not distinguish them here. Table II shows that there is a good match between theory and experiment. In fact, the main difference is near constant offset, which can be caused by the choice of the reference layer in DFT. In consequence, experiment and theory support each other and make further analysis reliable.

As often found the agreement for the coherent position P^H is significantly better than for the coherent fraction f^H as the former is a more robust parameter in experiment as explained above. That said, the experimental value found for the component S1 is particularly low, which indicates that also sulfur atoms other than those in the lower S layer of TaS$_2$ are collected in the XPS signal. Obvious candidates are S atoms adsorbed directly on Au(111) or found at island edges or in grain boundaries. It is puzzling that still the match for P^H is as good as for Ta and S2, which could be due to a fortuitous cancellation of the coherent positions of the impurities.

Details of the geometry determined by DFT can be found in Table III. The minimum height of the S1 atoms is observed in the regions where they reside directly above a gold substrate atom. For the other regions, the distance is larger, resulting in a corrugation amplitude of 0.33 Å for Ta$_{fcc}$S$_{top}$. The Ta layer and the upper S layer (S2) follow the lower layer with very similar corrugation. Averaging over all species and stackings the corrugation amplitude determined by DFT is $\Delta h_{DFT} \approx 0.3$ Å which is below the upper bound given by XSW. The average thickness of the TaS$_2$ monolayer (defined as the S-S distance) is 3.06 Å, which is comparable to the 3.11 Å value found for bulk 2H-TaS$_2$ [42].

We used the calculated structures for a simulation of STM images (not shown here; see Ref. [15]). The regions where S

occupies the top position [Ta$_{hcp}$S$_{top}$/Ta$_{fcc}$S$_{top}$, i.e., the center of the unit cell in Fig. 4(a)] that are closest to the Au(111) substrate are actually imaged highest (brightest color) in STM (center of the unit cell in Fig. 1). In other words, the STM contrast is inverted with respect to the topography. The corrugation observed in STM must therefore be dominated by electronic effects and cannot be directly related to the geometric corrugation measured by XSW and DFT.

Our theoretical results are in line with previous studies, where the height of S1 was reported as 2.37 Å [9] and 2.431 Å [8]. In these calculations, a simplified ($\sqrt{3} \times \sqrt{3}$) geometry was used, which does not allow one to study moiré-related spatial variations of the structure. Other 2DMs show a much larger corrugation amplitude, for example, hBN/Ir(111) ($\Delta h \approx 1.5$ Å [26]), so we can regard TaS$_2$ as a rather flat overlayer.

Figure 4(c) shows the charge transfer between the surface and the TaS$_2$ layer. Overall, 0.09 e$^-$ are transferred from Au(111) to each 2H-TaS$_2$ unit cell. Pronounced increase in negative charge is visible in the Ta d orbitals with no significant variation with atomic registry. In addition, for S on top of Au, charge accumulation between the atoms is found, a fingerprint of a covalentlike bond.

The overall charge transfer per TaS$_2$ unit cell is very similar as calculated by others (0.08 e$^-$ [8,9]) using simplified models. The conduction band of 2H-TaS$_2$ is formed by the Ta d orbitals, especially close to the Fermi level. Here, the out-of-plane d_{z^2} orbitals are the main contribution [43]. The charge increase observed in the plane of the Ta atoms can thus be interpreted as charge transfer into the conduction band of TaS$_2$. This also explains the homogenous charge distribution with respect to Ta in different registries. In analogy with MoS$_2$/Au(111) [44], we interpret the charge accumulation between S and Au in the Ta$_{fcc}$S$_{top}$ region as a chemical S-Au bond formed by overlapping S p_z and Au d orbitals.

IV. CONCLUSIONS

In conclusion, XSW enables a precise analysis of the vertical structure of 2H-TaS$_2$/Au(111) and is therefore the ideal counterpart of STM, which determines the lateral geometry with atomic resolution. The three different species in TaS$_2$ (lower S, middle Ta, upper S) can be clearly distinguished in XPS, a key requisite for a concise analysis in XSW. We find a good agreement between structural parameters found by XSW and DFT. The two rotational variants are geometrically very similar, and in consequence also show little difference in binding energy. Locally, covalentlike bonds between S atoms in the lower layer and Au substrate atoms form, but still the ultrathin layer only shows a small corrugation (≈ 0.3 Å in DFT, < 0.8 Å in XSW). We find significant charge transfer from Au(111) to TaS$_2$ that partially goes into the conduction band of the 2DM.

[1] M. Chhowalla, H. S. Shin, G. Eda, L. J. Li, K. P. Loh, and H. Zhang, The chemistry of two-dimensional layered transition metal dichalcogenide nanosheets, Nat. Chem. **5**, 263 (2013).

[2] N. F. Hinsche and K. S. Thygesen, Electron–phonon interaction and transport properties of metallic bulk and monolayer transition metal dichalcogenide TaS_2, 2D Mater. **5**, 015009 (2018).

[3] J. Shi, X. W. Wang, S. Zhang, L. Xiao, Y. Huan, Y. Gong, Z. Zhang, Y. Li, X. Zhou, M. Hong, Q. Fang, Q. Zhang, X. Liu, L. Gu, Z. Liu, and Y. Zhang, Two-dimensional metallic tantalum disulfide as a hydrogen evolution catalyst, Nat. Commun. **8**, 958 (2017).

[4] H. Lin, W. Huang, K. Zhao, C. Lian, W. Duan, X. Chen, and S.-H. Ji, Growth of atomically thick transition metal sulfide films on graphene/6H-SiC(0001) by molecular beam epitaxy, Nano Res. **11**, 4722 (2018).

[5] J. Hall, N. Ehlen, J. Berges, E. van Loon, C. van Efferen, C. Murray, M. Rösner, J. Li, B. V. Senkovskiy, M. Hell, M. Rolf, T. Heider, M. C. Asensio, J. Avila, L. Plucinski, T. Wehling, A. Grüneis, and T. Michely, Environmental control of charge density wave order in monolayer 2H-TaS_2, ACS Nano **13**, 10210 (2019).

[6] W. Fu, J. Qiao, X. Zhao, Y. Chen, D. Fu, W. Yu, K. Leng, P. Song, Z. Chen, T. Yu, S. J. Pennycook, S. Y. Quek, and K. P. Loh, Room temperature commensurate charge density wave on epitaxially grown bilayer 2H-tantalum sulfide on hexagonal boron nitride, ACS Nano **14**, 3917 (2020).

[7] Q. Zhang, L. Y. Gan, Y. Cheng, and U. Schwingenschlögl, Spin polarization driven by a charge-density wave in monolayer 1T-TaS_2, Phys. Rev. B **90**, 081103(R) (2014).

[8] F. Li and Q. Tang, Modulating the electronic structure and in-plane activity of two-dimensional transition metal dichalcogenide (MoS_2, TaS_2, NbS_2) monolayers by interfacial engineering, J. Phys. Chem. C **124**, 8822 (2020).

[9] B. Shao, A. Eich, C. Sanders, A. S. Ngankeu, M. Bianchi, P. Hofmann, A. A. Khajetoorians, and T. O. Wehling, Pseudodoping of a metallic two-dimensional material by the supporting substrate, Nat. Commun. **10**, 180 (2019).

[10] C. Busse, P. Lazić, R. Djemour, J. Coraux, T. Gerber, N. Atodiresei, V. Caciuc, R. Brako, A. T. N'Diaye, S. Blügel, J. Zegenhagen, and T. Michely, Graphene On Ir(111): Physisorption With Chemical Modulation, Phys. Rev. Lett. **107**, 036101 (2011).

[11] Q. Zhang, J. Yu, P. Ebert, C. Zhang, C.-R. Pan, M.-Y. Chou, C.-K. Shih, C. Zeng, and S. Yuan, Tuning band gap and work function modulations in monolayer hBN/Cu(111) heterostructures with moiré patterns, ACS Nano **12**, 9355 (2018).

[12] C. E. Sanders, M. Dendzik, A. S. Ngankeu, A. Eich, A. Bruix, M. Bianchi, J. A. Miwa, B. Hammer, A. A. Khajetoorians, and P. Hofmann, Crystalline and electronic structure of single-layer TaS_2, Phys. Rev. B **94**, 081404(R) (2016).

[13] O. R. Albertini, A. Y. Liu, and M. Calandra, Effect of electron doping on lattice instabilities in single-layer 1H-TaS_2, Phys. Rev. B **95**, 235121 (2017).

[14] H. M. Lefcochilos-Fogelquist, O. R. Albertini, and A. Y. Liu, Substrate-induced suppression of charge density wave phase in monolayer 1H-TaS_2 on Au(111), Phys. Rev. B **99**, 174113 (2019).

[15] D. Dombrowski, A. Samad, C. Murray, M. Petrović, P. Ewen, T. Michely, M. Kralj, U. Schwingenschlögl, and C. Busse, Two phases of monolayer tantalum sulfide on Au(111), ACS Nano **15**, 13516 (2021).

[16] S. G. Sørensen, H. G. Füchtbauer, A. K. Tuxen, A. S. Walton, and J. V. Lauritsen, Structure and electronic properties of in situ synthesized single-layer MoS_2 on a gold surface, ACS Nano **8**, 6788 (2014).

[17] S. S. Grønborg, S. Ulstrup, M. Bianchi, M. Dendzik, C. E. Sanders, J. V. Lauritsen, P. Hofmann, and J. A. Miwa, Synthesis of epitaxial single-layer MoS_2 on Au(111), Langmuir **31**, 9700 (2015).

[18] S. Doniach and M. Sunjic, Many-electron singularity in x-ray photoemission and x-ray line spectra from metals, J. Phys. C: Solid State Phys. **3**, 285 (1970).

[19] D. A. Shirley, High-resolution X-ray photoemission spectrum of the valence bands of gold, Phys. Rev. B **5**, 4709 (1972).

[20] J. Zegenhagen, Surface structure determination with x-ray standing waves, Surf. Sci. Rep. **18**, 202 (1993).

[21] D. P. Woodruff, Normal x-ray standing wave determination, Prog. Surf. Sci. **57**, 1 (1998).

[22] D. P. Woodruff, Surface structure determination using x-ray standing waves, Rep. Prog. Phys. **68**, 743 (2005).

[23] S. Runte, P. Lazić, C. Vo-Van, J. Coraux, J. Zegenhagen, and C. Busse, Graphene buckles under stress: An x-ray standing wave and scanning tunneling microscopy study, Phys. Rev. B **89**, 155427 (2014).

[24] J. Sforzini, L. Nemec, T. Denig, B. Stadtmüller, T.-L. Lee, C. Kumpf, S. Soubatch, U. Starke, P. Rinke, V. Blum, F. C. Bocquet, and F. S. Tautz, Approaching Truly Freestanding Graphene: The Structure of Hydrogen-Intercalated Graphene On 6H-SiC(0001), Phys. Rev. Lett. **114**, 106804 (2015).

[25] J. Sforzini, P. Hapala, M. Franke, G. van Straaten, A. Stöhr, S. Link, S. Soubatch, P. Jelínek, T.-L. Lee, U. Starke, M. Švec, F. C. Bocquet, and F. S. Tautz, Structural and Electronic Properties of Nitrogen-Doped Graphene, Phys. Rev. Lett. **116**, 126805 (2016).

[26] F. H. Farwick zum Hagen, D. M. Zimmermann, C. C. Silva, C. Schlueter, N. Atodiresei, W. Jolie, A. J. Martínez-Galera, D. Dombrowski, U. A. Schröder, M. Will, P. Lazić, V. Caciuc, S. Blügel, T.-L. Lee, T. Michely, and C. Busse, Structure and growth of hexagonal boron nitride on Ir(111), ACS Nano **10**, 11012 (2016).

[27] M. Schwarz, A. Riss, M. Garnica, J. Ducke, P. S. Deimel, D. A. Duncan, P. K. Thakur, T.-L. Lee, A. P. Seitsonen, J. V. Barth, F. Allegretti, and W. Auwärter, Corrugation in the weakly interacting hexagonal-BN/Cu(111) system: Structure determination by combining noncontact atomic force microscopy and X-ray standing waves, ACS Nano **11**, 9151 (2017).

[28] C. Brülke, T. Heepenstrick, N. Humberg, I. Krieger, M. Sokolowski, S. Weiß, F. S. Tautz, and S. Soubatch, Long vertical distance bonding of the hexagonal boron nitride monolayer on the Cu(111) surface, J. Phys. Chem. C **121**, 23964 (2017).

[29] C. C. Silva, M. Iannuzzi, D. A. Duncan, P. T. Ryan, K. T. Clarke, J. T. Küchle, J. Cai, W. Jolie, C. Schlueter, T.-L. Lee, and C. Busse, Valleys and hills of graphene on Ru(0001), J. Phys. Chem. C **122**, 18554 (2018).

[30] C. C. Silva, J. Cai, W. Jolie, D. Dombrowski, F. H. Farwick zum Hagen, A. J. Martínez-Galera, C. Schlueter, T.-L. Lee, and C. Busse, Lifting epitaxial graphene by intercalation of alkali metals, J. Phys. Chem. C **123**, 13712 (2019).

[31] M. J. Bedzyk and G. Materlik, Two-beam dynamical diffraction solution of the phase problem: A determination with x-ray standing-wave fields, Phys. Rev. B **32**, 6456 (1985).

[32] D. P. Woodruff and D. A. Duncan, X-ray standing wave studies of molecular adsorption, New J. Phys. **22**, 113012 (2020).

[33] B. W. Batterman, Effect of dynamical diffraction in X-ray fluorescence scattering, Phys. Rev **133**, A759 (1964).

[34] A. Maeland and T. B. Flanagan, Lattice spacings of gold–palladium alloys, Can. J. Phys. **42**, 2364 (1964).

[35] G. Mercurio, O. Bauer, M. Willenbockel, N. Fairley, W. Reckien, C. H. Schmitz, B. Fiedler, S. Soubatch, T. Bredow, M. Sokolowski, and F. S. Tautz, Adsorption height determination of nonequivalent C and O species of PTCDA on Ag(110) using x-ray standing waves, Phys. Rev. B **87**, 045421 (2013).

[36] G. Kresse and D. Joubert, From ultrasoft pseudopotentials to the projector augmented-wave method, Phys. Rev. B **59**, 1758 (1999).

[37] J. P. Perdew, K. Burke, and M. Ernzerhof, Generalized Gradient Approximation Made Simple, Phys. Rev. Lett. **77**, 3865 (1996).

[38] S. Grimme, J. Antony, S. Ehrlich, and H. Krieg, A consistent and accurate ab initio parametrization of density functional dispersion correction (DFT-D) for the 94 elements H-Pu, J. Chem. Phys. **132**, 154104 (2010).

[39] W. Tang, E. Sanville, and G. Henkelman, A grid-based Bader analysis algorithm without lattice bias, J. Phys.: Condens. Matter **21**, 084204 (2009).

[40] J. Coraux, A. T. N'Diaye, C. Busse, and T. Michely, Structural coherency of graphene on Ir(111), Nano Lett. **8**, 565 (2008).

[41] A. T. N'Diaye, J. Coraux, T. N. Plasa, C. Busse, and T. Michely, Structure of epitaxial graphene on Ir(111), New J. Phys. **10**, 043033 (2008).

[42] A. Meetsma, G. A. Wiegers, R. J. Haange, and J. L. de Boer, Structure of 2*H*-TaS$_2$, Acta Crystallogr. C **46**, 1598 (1990).

[43] A. V. Kolobov and J. Tominaga, *Two-Dimensional Transition-Metal Dichalcogenides* (Springer International Publishing AG Switzerland, Cham, 2016).

[44] A. Bruix, J. A. Miwa, N. Hauptmann, D. Wegner, S. Ulstrup, S. S. Grønborg, C. E. Sanders, M. Dendzik, A. Grubišić Čabo, M. Bianchi, J. V. Lauritsen, A. A. Khajetoorians, B. Hammer, and P. Hofmann, Single-layer MoS$_2$ on Au(111): Band gap renormalization and substrate interaction, Phys. Rev. B **93**, 165422 (2016).